AO4ELT7 - June 2023 - Avignon

AO3k at Subaru: the facility adaptive optics goes extreme

Julien Lozi[a], Kyohoon Ahn[a], Alicia Chun[b], Christophe Clergeon[c], Vincent Deo[a], Olivier Guyon[a,d,e,f], Takashi Hattori[a], Yosuke Minowa[a], Shogo Nishiyama[g], Yoshito Ono[a], and Sébastien Vievard[a,f]

[a]Subaru Telescope, National Astronomical Observatory of Japan, National Institutes of Natural Sciences (NINS), 650 North A'ohōkū Place, Hilo, HI 96720, United States
[b]University of Chicago, 5801 S. Ellis Ave., Chicago, IL 60637, United States
[c]Gemini International Observatory, a program of NSF's NOIRlab, 670 North A'ohōkū Place, Hilo, HI 96720, United States
[d]Steward Observatory, University of Arizona, Tucson, AZ 87521, United States
[e]College of Optical Sciences, University of Arizona, Tucson, AZ 87521, United States
[f]Astrobiology Center of NINS, 2 Chome-21-1, Osawa, Mitaka, Tokyo, 181-8588, Japan
[g]Miyagi University of Education, 149, Aramaki-aza-Aoba, Aobaku, Sendai

ABSTRACT

The facility adaptive optics of the Subaru Telescope AO188 is getting some long-awaited upgrades: a new 3224-actuator deformable mirror (DM) from ALPAO (hence the name change to AO3000 or AO3k), an upgraded GPU-based real-time computer, a non-linear curvature wavefront sensor and a near-infrared wavefront sensor (NIR WFS) using First Light Imaging's C-RED ONE camera, closing the loop at up to 2 kHz. With these new features, AO3k will provide extreme-AO level of correction to all the instruments on the IR Nasmyth platform: The NIR-MIR camera and spectrograph IRCS, the high-resolution Doppler spectrograph IRD, and the high-contrast instrument SCExAO. AO3k will also support laser tomography (LTAO), delivering high Strehl ratio imaging with large sky coverage.

Further author information: (Send correspondence to J.L.)
J.L.: E-mail: lozi@naoj.org, Telephone: 1 808 934 5949

The NIR WFS, using part of the light from y- to H-band, will dramatically increase the number of reachable targets for high-contrast imaging, for exoplanets characterization, as well as AGNs or the galactic center. It has two modes that can be used to drive the new DM: A double roof-prism pyramid WFS, and a focal plane WFS.

The high Strehl will especially benefit SCExAO for high contrast imaging. The second stage ExAO will no longer have to chase large residual atmospheric turbulence, and will focus on truly high contrast techniques to create and stabilize dark holes, as well as coherent differential imaging techniques. We will finally be able to leverage the several high performance coronagraphs tested in SCExAO, even in the visible.

AO3k will answer crucial questions as a precursor for future adaptive optics systems for ELTs, especially as a technology demonstrator for the HCI Planetary Systems Imager on the Thirty Meter Telescope. A lot of questions are still unanswered on the on-sky behavior of high actuator counts DMs, NIR wavefront sensing, the effect of rolling shutters or persistence.

We present here the first lab and on-sky results of AO3k, focusing mainly on the commissioning of the NIR WFS due to the delay in the delivery of the DM. These results give us some insight on the great scientific results we hope to achieve in the future.

Keywords: NIR wavefront sensor, extreme adaptive optics, non-linear curvature wavefront sensor, high-contrat imaging

1. INTRODUCTION

The first generations of adaptive optics (AO) and extreme AO (XAO) are getting upgraded with a larger number of actuators, faster low-noise detectors, more sensitive wavefront sensors (WFS) and even new near-infrared WFS (NIR WFS).

At the Subaru Telescope, following the success of the first AO system AO36, AO188 was developed and installed in 2006[15], including a laser guide star[5]. With 188 actuators in the pupil, AO188 can provide Strehl ratios of $\sim$ 20–40% in H-band in median seeing[12]. Three instruments are using the output of AO188:

- The facility instrument IRCS (Infrared Camera and Spectrograph), providing both imaging (y- to M'-bands) and spectroscopy (zJ- to L-band) capabilities.
- The PI XAO platform SCExAO (Subaru Coronagraphic Extreme Adaptive Optics), feeding several science modules in visible (R- and i-band) and NIR (y- to K-band), including the integral field spectrograph CHARIS, the MKID Exoplanet Camera (MEC) and the visible differential polarimetric imager VAMPIRES[6, 10].
- the PI instrument IRD (Infrared Doppler spectrograph), a NIR (y- to H-band) fiber-fed high resolution spectrograph. IRD can be fed directly with multi-mode fibers from AO188, or with single-mode fibers from SCExAO (REACH module)[7].

In the broader context of Subaru 2*, aiming at enhancing Subaru's functionalities in key aspects, such as wide-field, high-resolution observations and infrared astronomy, we want to push for better and faster wavefront control by upgrading components of AO188, SCExAO, and the whole instrument architecture of the infrared Nasmyth platform of Subaru. Finally, we want to test technologies necessary to prepare for the next generation of giant segmented telescopes like the Thirty Meter Telescope (TMT)[13].

In this paper, we will first present the steps envisioned to upgrade the facility adaptive optics and the instrument configuration (Sec. 2). Then we will detail the design and integration of the NIR WFS (Sec. 3). We will show the first on-sky results obtained in a passive setup (Sec. 4), and closing the loop on AO188's bimorph DM (Sec. 5). Finally, we will conclude and give some perspective to the work ahead of us.

*Subaru 2 website: https://subarutelescope.org/jp/subaru2/

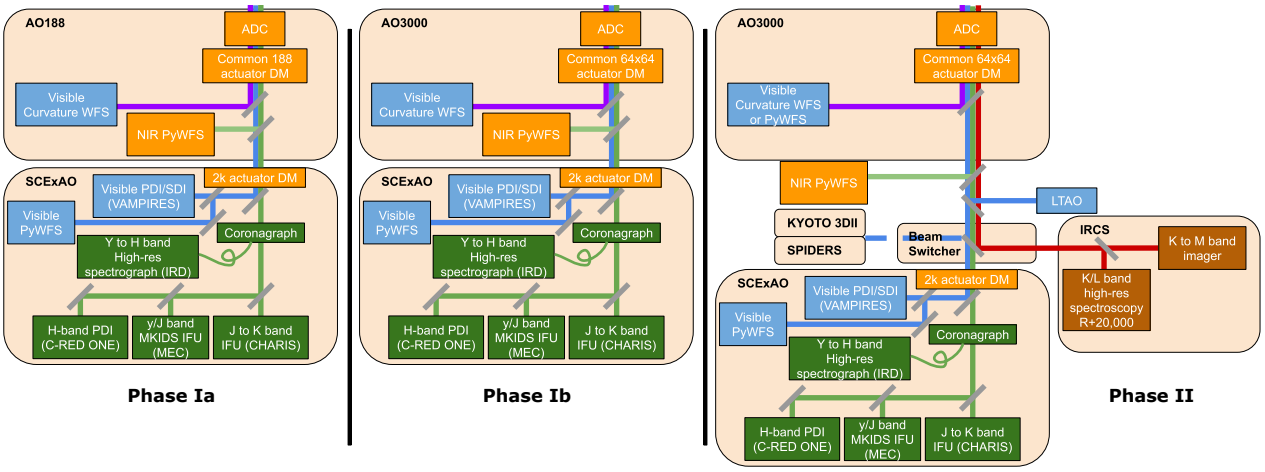

Figure 1. Phases of upgrades to the facility adaptive optics AO188 to AO3k. Phase Ia: addition of a NIR WFS inside AO188. Phase Ib: Replacement of the DM to ALPAO's 64x64. Phase II: Addition of a NasIR beam switcher to split the light between instruments.

2. AO3k: AN UPGRADE OF AO188 IN PHASES

The current facility adaptive optics of the Subaru Telescope AO188 is composed of a 188-actuator bimorph DM from Cilas, coupled with a visible curvature wavefront sensor using avalanche photo-diodes (APDs). A vibrating membrane modulate the signal at 2 kHz, So the loop runs at 1 kHz. It provides Strehl ratios between 20 and 40% in H-band in median seeing.

Higher performances are now becoming essential to improve the scientific output of the instruments using AO, by reaching deeper contrasts for high-contrast imagers, reaching fainter targets for imaging and spectroscopy, and reaching redder targets (M-type stars, stars embedded in dust, e.g. with protoplanetary rings, or around the galactic center)

The goal is to upgrade the facility adaptive optics in phases, with minimal impact on the observing schedule and current functionalities.

- **Phase Ia: Addition of a NIR WFS** (see Fig. 1 left).

  The goal of this phase is to add a NIR WFS inside the existing enclosure, without affecting the current AO188 performances and functionalities. This is the main focus of this paper. It was integrated inside AO188 for the first time in May 2022, and tested on-sky during some engineering time in May 2022 and May 2023. In 2022,we only operated the NIR WFS in a passive way, while closing the loop with the current visible CWFS. In 2023, we performed the first closed-loop tests using the 188-actuator bimorph DM. Thanks to these on-sky tests, the NIR WFS is now available for open-use observations starting in S24A.

- **Phase Ib: Replacement of the original 188-actuator DM with ALPAO's 64x64 DM**[16] (see Fig. 1 middle).

  In this phase, the number of available actuators in the pupil will increase from 188 to ~ 3000. Therefore, AO1888 will be re-branded as AO3k. After multiple delays due to the challenges in building such a large DM with thousands of actuators, The DM replacement is expected to be delivered in December 2023 and tested soon after, although the priority will be to maintain the current performance of AO188 by down-sampling the DM and using the current APDs for wavefront control.

  The new DM is a drop-in replacement of the original one, although the original one is also mounted on a fast tip/tilt mount where offloads of these modes are sent. Therefore, the fast tip/tilt mount will be equipped with a flat mirror and moved to the fold mirror right before the DM. Since the tip/tilt will not

be in a pupil plane anymore, the largest motions will be offloaded to the telescope's IRM2 mirror more regularly than before (typically every tens of seconds instead of every tens of minutes).

The visible curvature WFS will be upgraded with a non-linear version of the sensor using a sCMOS camera and imaging simultaneously four out-of-focus pupil images. This new WFS is still in an experimental phase, and will be tested on-sky at the end of 2023.

- **Phase II: Installation of a NasIR beam switcher for up to 4 instruments** (see Fig. 1 right).

  A NasIR beam switcher (NBS) is in its final design phase, allowing to switch rapidly between up to 4 instruments, and even splitting the light between 2 instruments (e.g. SCExAO and IRCS) with a dichroic beamsplitter.

  In this phase, the NIR WFS will move out of AO3k, on a common platform with the laser tomography AO (LTAO) currently in development, a precursor of the future MCAO ULTIMATE-SUBARU. In this configuration, the NIR WFS will be equipped with a pickoff wheel that will host the various dichroic beamsplitters described in the next section.

3. NIR WFS DESIGN AND INTEGRATION

A NIR PyWFS was first envisioned in the development phase of AO188, based on the PYRAMIR system[2, 3], but it did not materialize at the time. It was not until the development of the photon-counting NIR SAPHIRA detector[1] that a NIR PyWFS was tested on the SCExAO instrument as a technology demonstration[11].

The opto-mechanical design of AO3k's NIR WFS was based on the legacy of SCExAO's visible pyramid WFS (PyWFS): the light from the guide star is collimated and the pupil reimaged on a fast tip/tilt modulator using a custom achromatic doublet ($f = 150$ mm, $\phi_{\text{pupil}} = 10.7$ mm), then it is refocused on the tip of a double-roof prism pyramid optics, using a pair of converging and diverging doublets ($f_1 = 150$ mm and $f_2 = -50$ mm). Finally, a pupil lens ($f = 80$ mm) reimages the four pupils on a fast camera (see Fig. 2 (a)).

With SCExAO, we demonstrated that the double-roof prism design was performing well, despite its chromatic nature. The NIR version is designed to work between y- and H-band (0.98 to 1.8 µm), while the visible one works between 0.6 and 0.9 µm. The visible one uses N-BK7 glass, while the NIR one uses CaF2 glass, for its lower chromaticity in infrared. In the end, both designs end up with a similar chromatic spread over their working range.

The camera used for wavefront sensing is the First Light Imaging C-RED ONE camera, a fast low-noise photon-counting device that is currently the most suited for this application. The camera was purchased for two applications: the NIR WFS described here, and a fast polarization differential imaging (FPDI) mode, that was tested and offered for Open-Use science in S21B[9]. The opto-mechanical design had to accommodate the fact

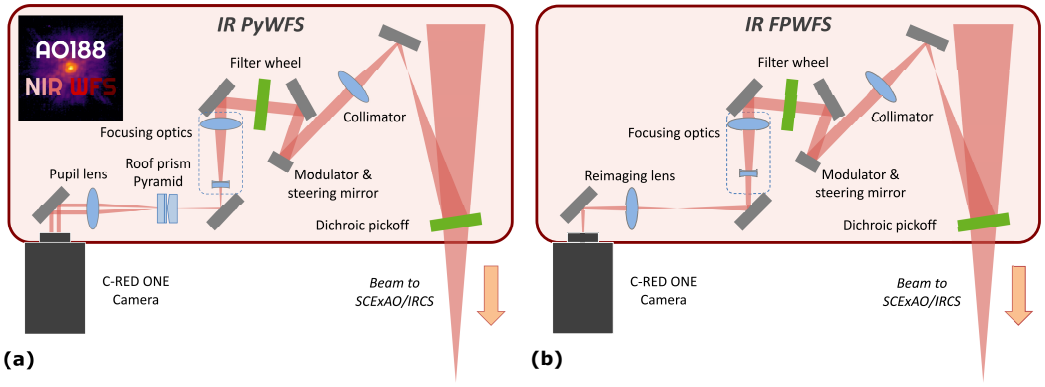

Figure 2. Diagram of the optical path of the NIR WFS inside AO18. (a) PyWFS mode. (b) FPWFS mode. A pupil viewing mode is also available by using the PyWFS mode and moving the pyramid optics out of the way.

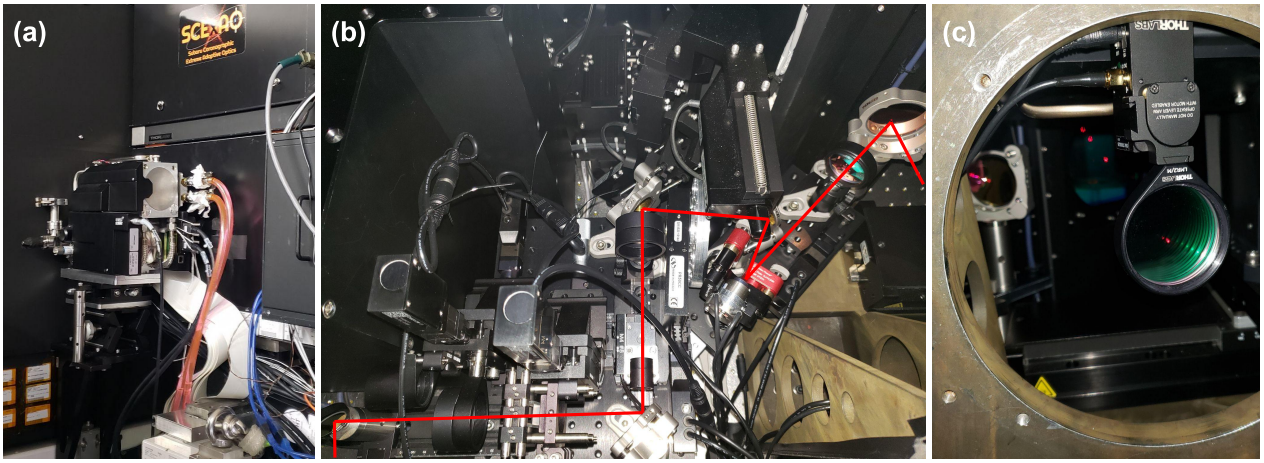

Figure 3. Integration of the NIR WFS inside AO188. (a) C-RED ONE camera sticking out of AO188, with SCExAO on its right. (b) NIR WFS core optics inside AO188. (c) NIR WFS dichroic beamsplitter in a flip mount, at the output port of AO188.

that the camera would physically need to be moved between two locations, although since then, we managed to purchase a second camera.

The main difference with SCExAO's PyWFS is that we need to be able to close the loop on off-axis natural guide stars. One application for the NIR WFS is the observation of the galactic center, where the closest guide star (GCIRS 7, $mag_H = 9.26$) is 5" away from Sgr A*. To be able to reach this type of targets, the modulator is mounted on a motorized tip/tilt mount, which allows to steer the line of sight of the NIR WFS. The mount is also used as a dithering mirror for the spectrogrpahic mode of IRCS.

Finally, during the design phase, it was decided to add a focal plane imaging mode to the NIR WFS for several reasons:

- It allows to calibrate the radius of modulation,
- It is useful to measure seeing before closing the loop,
- It can characterize the NIR point spread function (PSF) when the visible wavefront sensor is used,
- by adding defocus, it ca be used as a focal plane WFS on faint targets, unreachable with the PyWFS mode. This can eventually be useful as a truth WFS (tip/tilt and focus modes) for the LTAO.

The work on focal plane wavefront sensing is on-going with SCExAO, and is mostly based on the legacy of the Lyot-based Low-Order WFS (LLOWFS)[14] and mono-plane wavefront sensing[17].

The FPWFS mode is achieved simply by moving the pyramid optics out of the way, changing the pupil lens with a reimaging lens ($f = 150$ mm), and refocusing the diverging lens of the focusing optics (see Fig. 2 (b)). Thanks to this modularity, a simple pupil viewing mode is also available by using the PyWFS mode and moving the pyramid optics out of the way.

Mechanically, the difficulty was to have a compact design that uses the limited space inside AO188, without affecting the current components. It uses mainly off-the-shelf parts and motors, and very limited custom parts.

The design of the NIR WFS was completed in 2021. All the parts were procured and assembled in 2021 and beginning of 2022, and mounted inside AO188 for the first time in May 2022. Figure 3 shows the final result: (a) we can see the C-RED ONE camera mounted on a platform sticking out of AO188. On its right is the SCExAO instrument; (b) the core optics of the NIR WFS inside AO188, despite the tight space; (c) the dichroic beamsplitter sending part of the NIR light to the sensor. In this phase, only one beamsplitter can be mounted at a time in the motorized flip mount.

The wavelength range of the NIR WFS is defined by two optics: the dichroic beamsplitter and an internal filter wheel. The filter wheel contains the regular Maunakea band filters from ASAHI Spectra (y-, J- and H-band), as well as two custom filters combining respectively y- and J-band, and J- and H-band. Their throughputs are compiled in Fig. 4 (a). An open slot is also available to get the whole broadband mode, between y- and H-band. For the dichroic beamsplitters, we currently have four options. Their reflectance are presented in Fig. 4 (b). Their absorption is negligible, so the rest of the light goes to the science instrument. The four beamsplitters are:

- **K-band dichroic**: designed for IRCS K-band observations, it sends all of y- to H-band to the NIR WFS, and all of K-band to the science instrument. It can also be used for SCExAO/CHARIS K-band high-resolution IFS.
- **YJH50 dichroic**: It sends 50% of y- to H-band to the NIR WFS, and the other 50% to SCExAO or IRCS. It also transmit all of K-band and all of visible light (R- and I-bands) to the science modules, in the case of SCExAO.
- **YJH90 dichroic**: Similarly to the previous one, all of R-, I- ad K-band is transmitted, and only 10% of y- to H-band is reflected towards the NIR WFS. This dichroic is more suited for brighter targets, with only a small penalty for the science path.
- **Vis-HK dichroic**: This beamsplitter sends all of y- and J-band to the NIR WFS, and transmits all of R-, I-, H- and K-band for science.

Although each beamsplitter was designed for a specific instrument, they could be used by others if they are more suited. Once the NBS is installed for phase II, the NIR WFS will be able to migrate out of the AO3k enclosure, which will allow us to use a beamsplitter wheel instead of the flip mount. In that case, all the beamsplitters will be available without manual intervention. We may get other beamsplitter designs as well in the future, for example to allow L- & M-band observations.

The C-RED ONE camera is used in Correlated Double Sampling (CDS) mode, where the sub-frame is read immediately after a frame reset, then reset and read again. The result is the difference between the frame before the reset and the previous one just after the reset. The sub-frame used is 160x160 pixels, with a read time of $t_{\mathrm{read}} = 102$ µs. So if we program the CDS mode to run at a frequency F_{CDS}, then the actual integration time t_{int} will be

$$t_{\mathrm{int}} = \frac{1}{F_{\mathrm{CDS}}} - t_{\mathrm{read}}. \tag{1}$$

In that case, we do not want the modulator to be synchronized with the CDS reads, otherwise we would lose a fraction of the rotation cycle during the actual integration time. Therefore, the modulation frequency F_{mod} is set

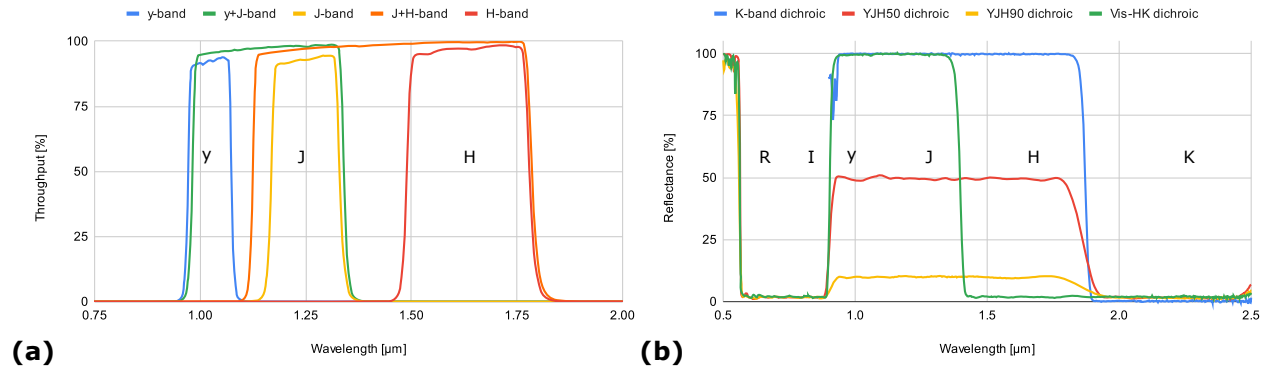

Figure 4. (a) Throughput of the filters inside the NIR WFS filter wheel. (b) Reflectivity of the NIR WFS dichroic pickoff options available.

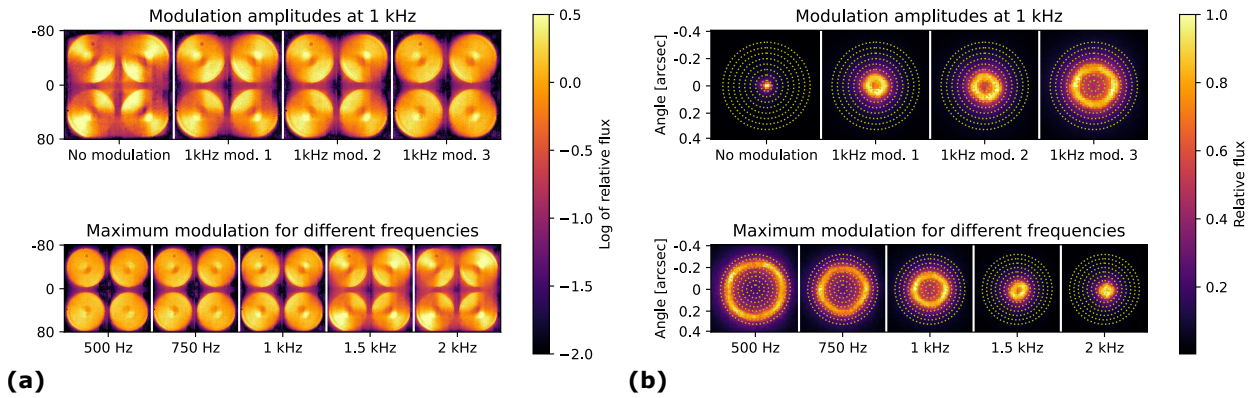

Figure 5. (a) PyWFS images for different frequencies and modulation using the internal laser source (1550 nm). The "flat" DM shows signs of astigmatism. (b) Different modulation parameters @1 kHz (top) and maximum modulation at different frequencies (bottom).

to

$$F_{\mathrm{mod}} = \frac{1}{t_{\mathrm{int}}} = \frac{F_{\mathrm{CDS}}}{1 - F_{\mathrm{CDS}} t_{\mathrm{read}}}. \tag{2}$$

Table 1 presents the integration time, modulator frequency and maximum modulation radius for various loop frequencies. The maximum frequency for CDS mode and the desired sub-window is 4.9 kHz, at which point the duty cycle drops to 50%. The readout scheme creates a rolling shutter effect linked to the duty cycle that is out of the scope of this paper, although we will probably always be at or below 2 kHz, where this effect will not impact us too much.

AO188 is only equipped with two laser diodes, one at 633 nm, and one at 1.55 µm, but lacks a proper broadband source. We are currently working on adding a broadband source, but for now, we could only use the NIR diode for internal testing. We programmed modulator parameters for the frequencies mentioned in Tab. 1, as well as three different amplitudes at 1 kHz. The modulator can always be turned off at any frequency.

Figure 5 presents results using the internal laser diode, (a) in PyWFS mode and (b) in focal plane mode. The PyWFS images are displayed in log scale to see the amount of light between the pupils. For the focal plane images, circles with radii steps of 40 mas (1 λ/D in H-band) were added to do a quick measurement of the modulation radii.

From Fig. 5 (a), we can notice a few things. First, the supposed "flat" map of the bimorph DM is not quite flat, some astigmatism is visible. Second, the actuators behind the central obstruction create an artifact on the wavefront at the center. These two points are probably due to the fact that the source is not perfectly aligned, and there is not pupil mask simulating the Subaru pupil when creating a flat map with the internal source. Besides that, we can see that there is a minimal amount of light between the pupils, even when the modulator is turned off, indicating a very good quality of the roof prism vertices. We can also notice that, as expected, the amount of

Table 1. Integration time, modulator frequency and maximum modulation radius for various loop frequencies.

CDS/loop frequency [Hz]	500	750	1000	1500	2000
Actual integration time [ms]	1.898	1.231	0.898	0.565	0.398
Modulator frequency [Hz]	526.9	812.1	1113.6	1771.0	2512.6
Duty cycle [%]	95	92	90	85	80
Maximum modulation radius [mas]	250	190	145	60	40

light outside of the pupils is reduced with increased modulation. Similarly, the contrast of the astigmatism mode is reduced with higher modulation.

On Fig. 5 (b), we can see the corresponding modulations in the focal plane. Some work is still needed at some frequencies to get more circular patterns, and also to be able to transition smoothly between modulation radii. In the future, we would like to be able to reduce the modulation on the fly, depending on the seeing and the quality of the correction, and potentially turn off the modulation.

4. FIRST ON-SKY TESTING OF THE NIR WFS

The testing with the lab source were very limited, due to the quality of the source, and the lack of broadband light. Figure 6 (a) present focal plane and pupil images without and with added defocus. The defocused pupil image shows the actuators of the bimorph DM, especially the effect of central actuators creating a ring of aberrations. The defocused focal plane image also shows that the image has some halo , maybe due to the diode itself.

The NIR WFS was tested on-sky for the first time during two engineering nights, on May 21 and May 24, 2022, in median seeing conditions (~ 0.6") for both nights. The SCExAO dichroic #1 (referred as the SCExAO dichroic hereafter) was the one used as the beamsplitter, allowing us the record visible and NIR telemetry with SCExAO in the background. We only managed to get about 2 hours of data due to high humidity. Despite the short amount of time, we acquired sufficient data to characterize all the modes. For safety reasons, no command from the NIR WFS was sent to the original bimorph DM, although the wavefront control loop was still closed using the visible curvature WFS.

Figure 6 (b) validates the pupil imaging mode: the pupil of Subaru, including the spider arms and central obstruction, are well conjugated. The pupil is about 68 pixels across, as expected. It was designed to over-sample slightly the new ALPAO DM, which should provide 60 to 62 actuators across the pupil diameter.

We took several telemetry datasets with the PyWFS, for various modes: with the AO188 loop open and closed, with the various filters available, as well as for different acquisition frequencies and modulation radii. In all cases, the PyWFS performed as expected. SCExAO telemetry (e.g. focal plane images in visible and NIR, visible PyWFS pseudo-open loop measurements) was acquired simultaneously, although some more work is needed to compare the results to the NIR PyWFS telemetry.

Figure 7 (a) presents 30-s averages at 1 kHz and 2 kHz, with the AO188 loop open and closed, at maximum modulation. In open-loop, what we see is not really the turbulence, as it averages over 30 s, but the shape of the DM before the loop was opened. Though it is a good indication of the amount of signal we would get in open-loop in median seeing.

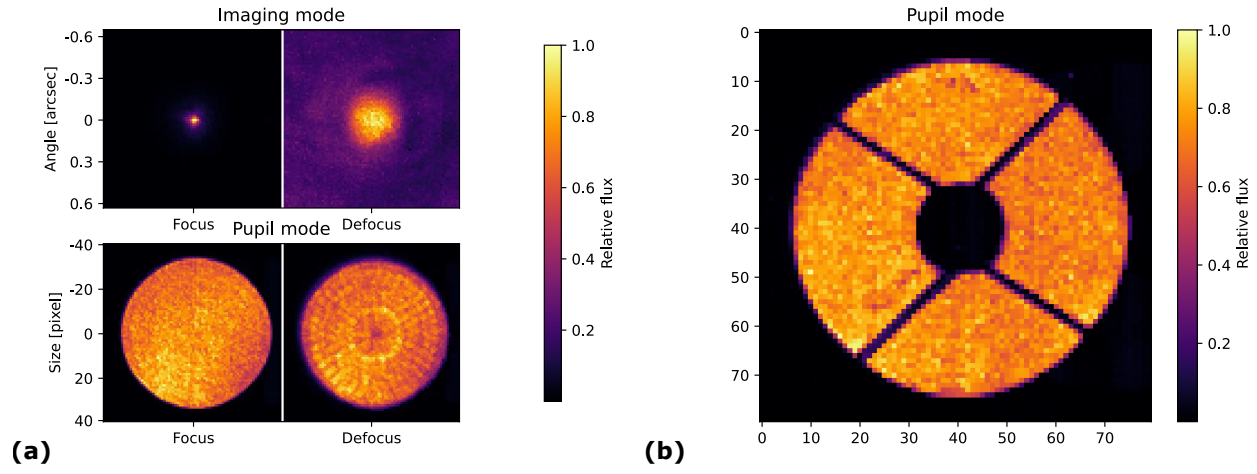

Figure 6. (a) Focal plane and pupil plane image in and out of focus, using the internal 1550 nm laser diode. (b) Pupil mode on-sky, in broadband mode (y- to H-band).

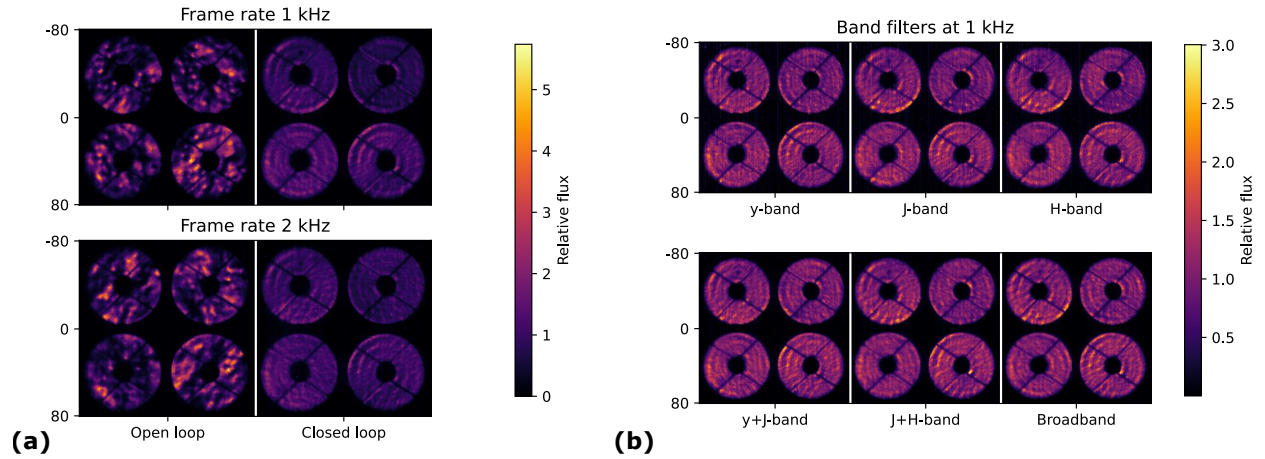

Figure 7. (a) AO188 loop open and closed. (b) PyWFS images with the various filters. Average of 30s of data for all cases.

Figure 7 (b) shows 30-s averages for each filter. There is no noticeable differences between the different filters and the broadband mode, demonstrating the good achromaticity of the optics, as well as the limited chromatic effects of the double-roof pyramid design. A more dynamical analysis of the data is on-going, especially comparing them to the visible PyWFS telemetry, although the lack of response matrix for the NIR PyWFS is limiting us.

Despite not being able to close the loop with the NIR PyWFS, we can still deduce limits in stellar magnitudes by comparing the signal-to-noise ratio (SNR) per pixel obtained for the known magnitude with the minimum SNR per pixel needed to close the loop with the visible PyWFS inside SCExAO. Indeed, with SCExAO, we are able to close the loop up to $m_I = 11$ stars, giving a minimum SNR per pixel of $S_{\rm min} = 0.12$.

For these measurements, we acquired data at 1 kHz on the A0V star HD 116160, which has a very flat magnitude of $m_\star = 5.6$ over all the bands of interest. First, the average flux in the illuminated parts of the image $F_{\rm ADU}$ is converted in electrons $F_{\rm e}$, by multiplying with the detector gain $g_{\rm det} = 0.45$ e$^-$/ADU and the amplification gain $g_{\rm amp} = 121$ for this camera, such as

$$F_{\rm e} = F_{\rm ADU} \times g_{\rm det} \times g_{\rm amp}. \tag{3}$$

Then the SNR per pixel $S_\star$ is calculated by considering both the readout noise (RON) measured from the dark files $\sigma_{\rm RON} = 0.12$ e$^-$ and the photon noise estimated from the flux $\sigma_{\rm ph} = \sqrt{F_{\rm e}}$, such as

$$S_\star = \frac{F_{\rm e}}{\sqrt{\sigma_{\rm ph}^2 + \sigma_{\rm RON}^2}} = \frac{F_{\rm e}}{\sqrt{F_{\rm e} + \sigma_{\rm RON}^2}}. \tag{4}$$

Finally, we find the magnitude limit at 1 kHz $m_{\rm lim,1kHz}$ by comparing this measured SNR to the assumed minimum SNR $S_{\rm min}$,

$$m_{\rm lim,1kHz} = m_\star + 5 \log \frac{S_\star}{S_{\rm min}}. \tag{5}$$

We can also interpolate this result for other frequencies f by adding $2.5 \log t_f / t_{\rm 1kHz}$ to the magnitude limit, where t_f is the actual exposure time at that frequency from Tab. 1. Finally, the magnitude limit for the other dichroics can also be interpolated by adding $2.5 \log R_{\rm dichroic}/R_{\rm YJH50}$, with $R_{\rm dichroic}$ and $R_{\rm YJH50}$ the reflectivity of the dichroic of interest and the the YJH50 dichroic used on-sky respectively.

Figure 8 (a) presents the calculated magnitude limits based on the datasets for each filter. The band filters give similar results, with magnitude limits around 10.5 for the YJH50 dichroic at 500 Hz, and around 11.3 for the K-band dichroic at the same frequency. With two bands, the magnitude limit increases by about one magnitude, and another half magnitude with all the light. Of course, this will depend heavily on the spectrum of the star: very red stars will provide light mostly in H-band for example. Similar magnitude limit estimations for the FPWFS mode are presented in [8].

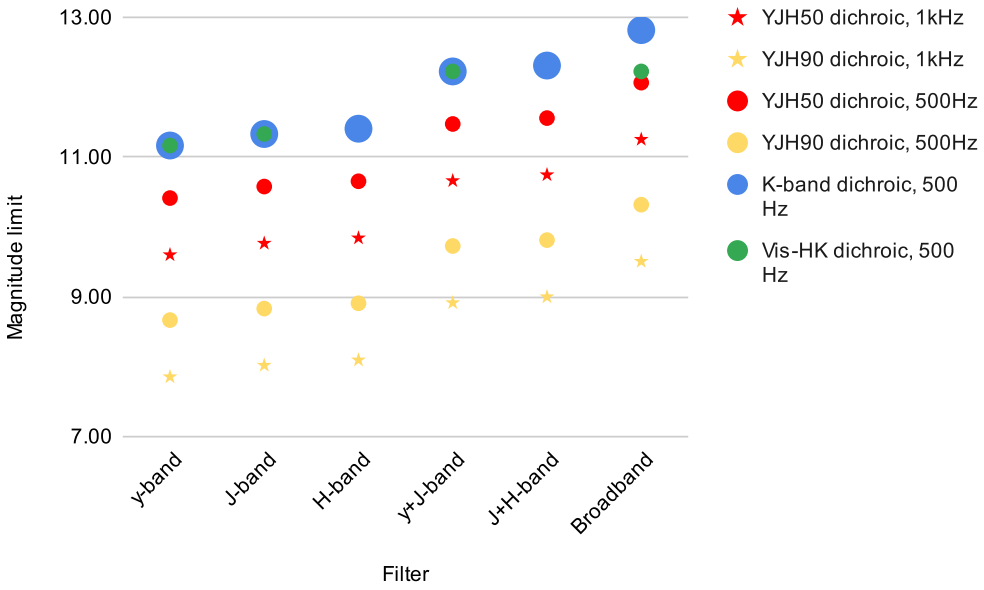

Figure 8. Estimated magnitude limit with the various filters, by matching the SNR per pixel to the visible PyWFS case.

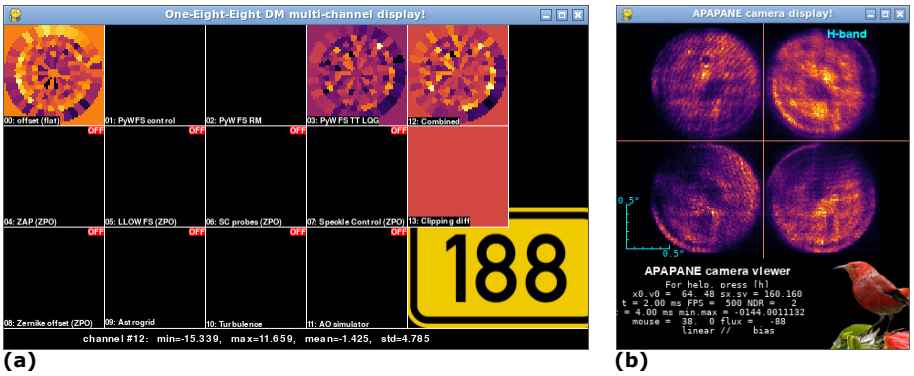

Figure 9. GUIs developed for SCExAO and recycled for the NIR WFS close-loop test: (a) DM display, with separate independent command channels that are added together and sent to the DM (right-most image). (b) 'Apapane camera display, showing the PyWFS image. Camera parameters are configured via keyboard shortcuts.

5. CLOSING THE LOOP WITH THE NIR WFS AND THE 188-ACTUATOR DM

5.1 Strategy and setup

Due to the delays in the delivery of the ALPAO 64x64 DM, we decided to first close the loop with the original 188-element bimorph DM of AO188. This presented an additional challenge, since the current Real-Time System (RTS) driving the 188-element DM is too old to run the NIR WFS loop. A new RTS was developed, based on the work of a previous unfinished upgrade that solved the communication with the the hardware, the SCExAO team's experience with CACAO[4] and the tools developed to control and display the C-RED ONE camera and the SCExAO DM.

Figure 9 presents examples of GUIs developed for the SCExAO DM and C-RED ONE camera, and adapted or simply reused for the NIR WFS. The actuators of the bimorph DM are significantly over-sampled on the C-RED ONE camera, compared to the 64x64 DM. The NIR WFS is therefore less sensitive to chromatic aberrations and pupil misalignments.

Once the new RTS was ready and we could communicate with the DM, we could start testing closing the loop with the NIR WFS. But first, the hardware latency was estimated by poking the DM. The hardware latency is the

time between receiving an image and the command being first applied to the DM. It has to be as small as possible. We measure it by sending commands to the deformable mirror with small incremental delays, and measuring changes in the sensor. The ideal response would then be a triangle function with a rising time corresponding to the integration time, and the hardware latency the time when we reach the half-way point. This latency is independent of the loop frequency.

Figure 10 present the latency measurements for two loop frequencies: at 500 Hz and 2 kHz. At both frequencies, we measured the hardware latency to be 0.5 ms, independently of the loop frequency as expected. This corresponds to 1 frame at 2 kHz, 0.5 frame at 1 kHz and 0.25 frame at 500 Hz. This is good, and should help in case of high wind. But we also noticed the strong mechanical resonance of the 188 DM at 1.2 kHz, which limits the control at 1 kHz, and makes control at 2 kHz unlikely with the current AO188 DM.

5.2 On-sky close-loop results with the NIR WFS and the 188-actuator DM

The on-sky results presented below where taken during the engineering night of May 3, 2023. We ran the AO loop at 500 Hz with the YJH50 dichroic beamsplitter. The seeing was above average: 0.7 to 1.1", with strong winds of 30 m.s^{-1} at high altitude. We observed several targets with similar magnitudes in J and H. Images were recorded with SCExAO's internal SWIR camera Palila (First Light Imaging C-RED 2, y- to H-band), and the CHARIS integral field spectrograph in broadband mode (J- to K-band).

Figure 11 (a) presents a sample of H-band images taken with Palila to measure the Strehl ratio, for several targets with various magnitudes. The targets were chosen in the same part of the sky to have similar atmospheric conditions for each of them. The airmass was between 1 and 1.4 for all of them, although the seeing was variable.

Figure 11 (b) shows a compilation of all the Strehl ratio measurements taken with Palila in y-, J- and H-band. This includes times where we were tuning various parameters, so some Strehl values can be much lower than optimal. The higher values for each magnitude would represent the performance of the loop in normal conditions. The Strehl ratio is over 40% until magnitude 9, then decreases. This was done with the YJH50 dichroic, so the result would be shifted by +0.75 magnitude with the K-band dichroic, and -1.75 with the YJH90 dichroic.

We can change the H-band filter in front of the Palila camera to a J-band or y-band filter, and look at the chromaticity of the correction. Figure 12 presents such results in the three bands for the same target. As expected, the Strehl ratio degrades at shorter wavelengths, but in all cases, a dark hole (control region of the deformable mirror) is visible, with diffraction rings and spider patterns. This is a sign that the correction is excellent, even better than with the curvature wavefront sensor for which this dark hole was never observed.

The data recorded with CHARIS was also analyzed, and gives us a more chromatic estimation of the Strehl, over J-, H- and K-band. Figure 13 presents such an analysis on the target X Boo. In this case slices of the

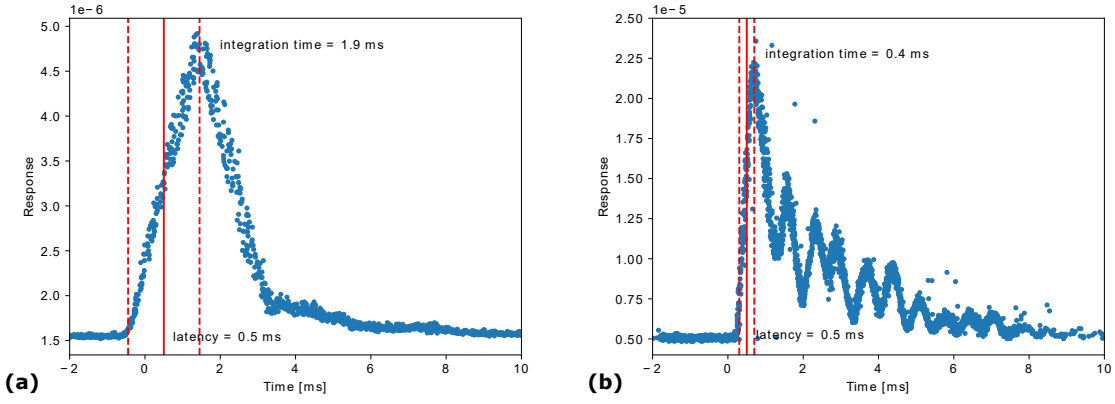

Figure 10. Hardware latency measurements for a loop speed of (a) 500 Hz and (b) 2 kHz. The rising time of the response corresponds to the integration time of the camera, while the half-way point corresponds to the frequency-independent hardware latency, in this case 0.5 ms.

CHARIS spectral cube are collapsed to form an image for each band, but the Strehl ratio is also measured independently for each slice. In the collapsed images, we can clearly see once again the control region of the DM. The spectral analysis of each slice is shown in Figure 14. This figure displays only the analysis of the best CHARIS exposure for each target observed during the engineering night. Most curves tend to plateau and even decrease after 2 µm, which is probably an effect of the increased thermal background that was not subtracted properly. Otherwise, the Strehl ratio evolves pretty linearly with wavelength. On this figure, nearly all the targets were in the same part of the sky, with similar conditions and airmass. The only outlier is GCIRS7, the brightest star around the galactic center. For this target, the correction was only marginal, despite being brighter than LP439-35. This can be attributed to the difference in airmass between the two targets, 1.6 and 1.07 respectively, and the strong wind speed that night.

We also tested the capacity to close the loop on an off-axis natural guide star on the binary system ξ Boo (separation 7.2"). On this target, we closed the loop on ξ Boo A, and steered the NIR WFS to center ξ Boo B in the field-of-view of SCExAO/CHARIS. Figure 15 presents the result of this test. The Strehl ratio on ξ Boo A is already degraded compared to other targets with similar magnitudes, probably due to the higher airmass (1.3), the strong high-altitude winds and the fact that we were closing the loop at 500 Hz. After the offset is applied, the analysis on ξ Boo B shows a strong wind-driven halo accentuated by the anisoplanetism. The Strehl ratio is consistently reduced by half in the three bands.

6. CONCLUSION AND PERSPECTIVE

To fully exploit the high-contrast imaging potential of the Subaru Telescope, the facility adaptive optics AO188 will receive well deserved upgrades. Despite some delays, we are making great progress towards upgrading AO188

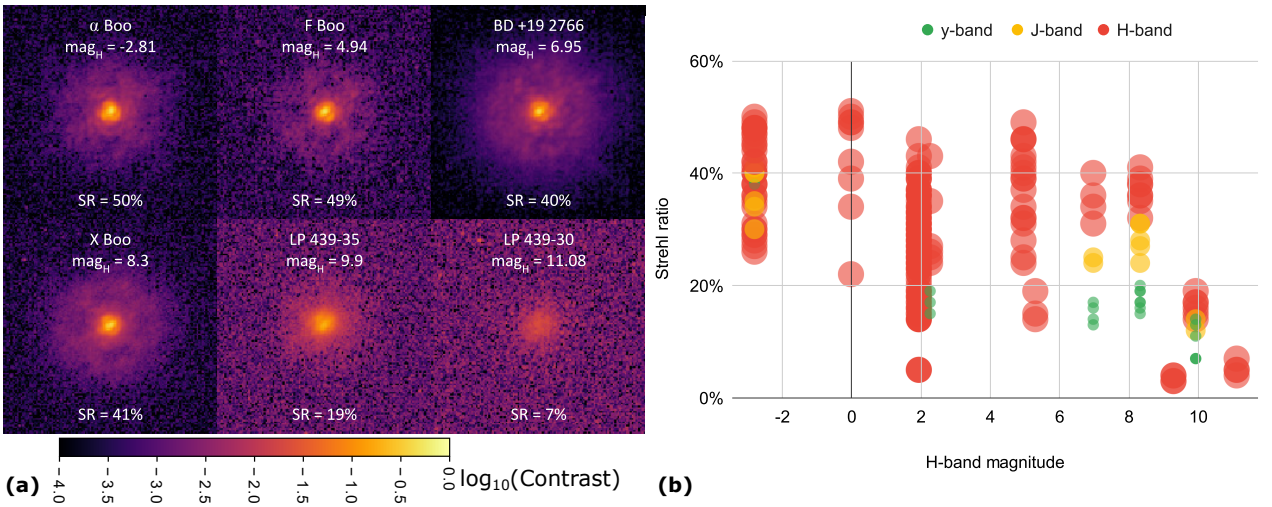

Figure 11. (a) H-band Strehl ratio measurements obtained with SCExAO's Palila camera, over a few seconds, for targets with various magnitudes. Each image is 2x2". (b) All Strehl ratio measurements taken with Palila in y-, J- and H-band.

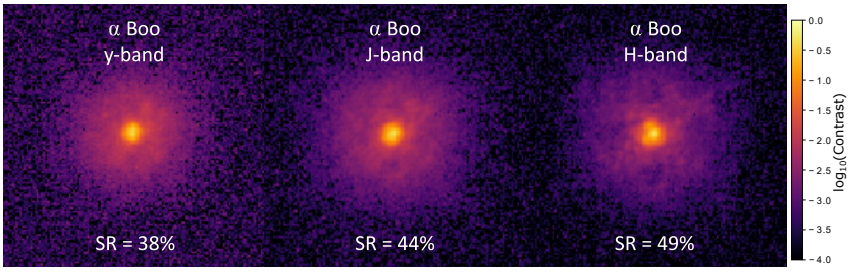

Figure 12. Strehl ratio measurements in y-, J- and H-band with SCExAO's Palila camera, on the target α Boo.

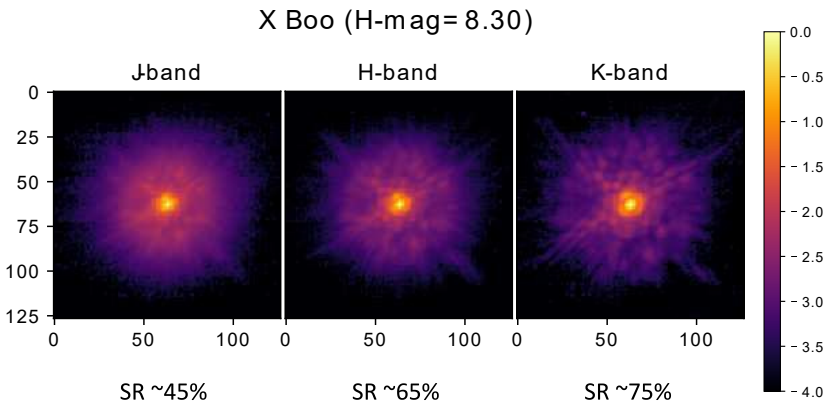

Figure 13. Strehl ratio measurements in J-, H- and K-band with CHARIS, on the target X Boo.

into AO3k, a XAO-level first stage adaptive optics with more than 3000 actuators in the pupil. The upgrades are happening in stages, to minimize the impact on current science observations. Once everything is in place, AO3k will feed multiple instruments thanks to a beam switcher, and even allow for simultaneous observations with two instruments.

In a first step, We successfully installed and tested on-sky for the first time a NIR WFS using a C-RED ONE camera. With the NIR WFS, we achieved the goal of adding two wavefront sensing capabilities (a pyramid WFS mode and a focal plane WFS mode) to AO188, without compromising any of its capabilities. The first on-sky tests, despite being brief and only in open-loop, taught us a lot about the future capabilities of this WFS. The PyWFS should be able to close the loop down to magnitudes 10 to 13, depending on the spectral type of the star and the mode used. The FPWFS should be able to reach even fainter stars, although more lab and on-sky work is needed to confirm these numbers.

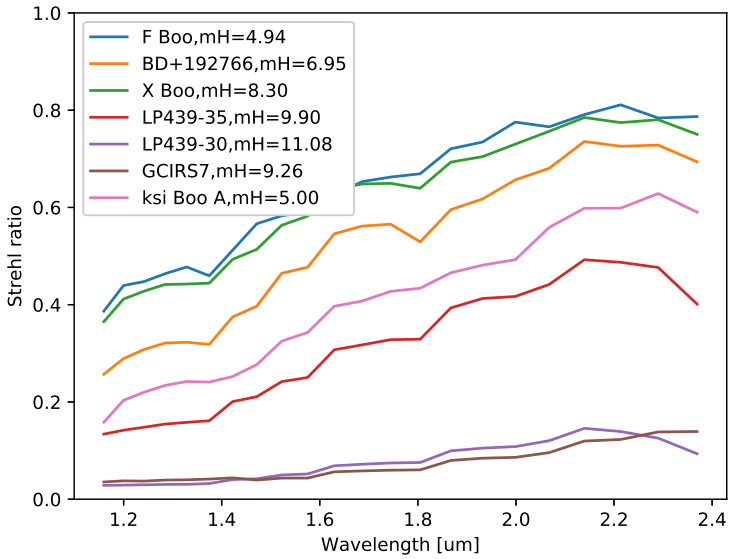

Figure 14. Strehl ratio measurements for the best frame of each target, for each wavelength slice of CHARIS in broadband mode.

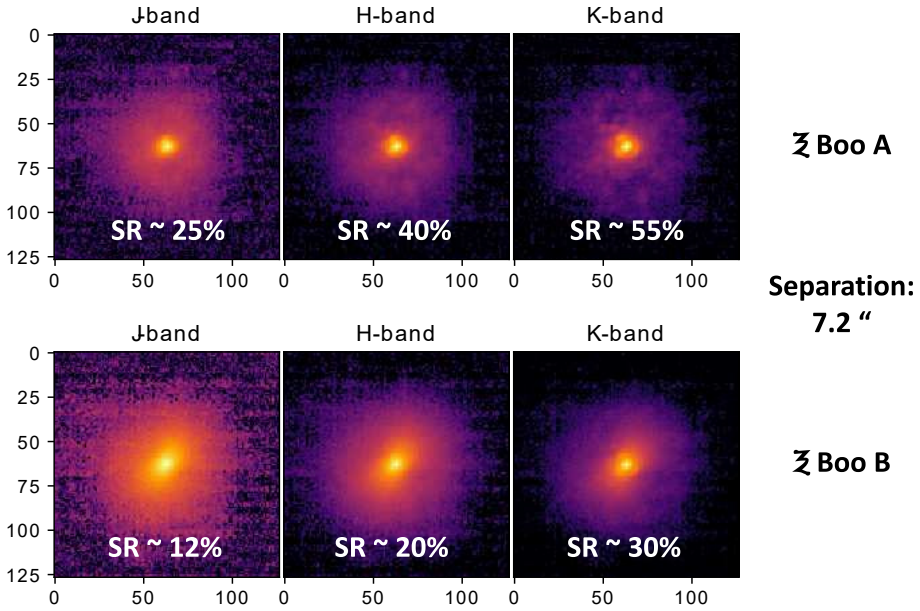

Figure 15. Strehl ratio measurements on the binary ξ Boo AB (H-mag 5 for both stars). The loop was closed on ξ Boo A, then the NIR WFS was steered on the companion ξ Boo B.

We performed the first on-sky closed-loop tests with the NIR WFS using the current 188-element DM, and demonstrated a very high quality of correction, despite the non-ideal atmospheric conditions, and the limited number of actuators: we are actually performing better than the current visible CWFS. These results allowed us to open the NIR WFS to the community, and will start science observations at the beginning of 2024.

Despite some delays in the delivery of the new 64x64-actuator DM, we should integrate it to the instrument in the next few months, and we expect to demonstrate ExAO level of performance thanks to the NIR WFS, and the new non-linear visible CWFS.

The next few years are truly going to be exciting for high-contrast imaging at the Subaru Telescope, as we will be able to reach deeper and more stable contrasts, around much redder targets. The technologies tested now will also be essential for the next generation of telescopes like TMT.

ACKNOWLEDGMENTS

The development of SCExAO & AO3k were supported by the Japan Society for the Promotion of Science (Grant-in-Aid for Research #23340051, #26220704, #23103002, #19H00703 & #19H00695), the Astrobiology Center of the National Institutes of Natural Sciences, Japan, the Mt Cuba Foundation and the director's contingency fund at Subaru Telescope. The authors wish to recognize and acknowledge the very significant cultural role and reverence that the summit of Maunakea has always had within the Hawaiian community. We are most fortunate to have the opportunity to conduct observations from this mountain. KA acknowledges funding from the Heising-Simons foundation. VD acknowledges support from NASA funding (Grant #80NSSC19K0336).

References

[1] Dani Atkinson et al. “Observatory deployment and characterization of SAPHIRA HgCdTe APD arrays”. In: *High Energy, Optical, and Infrared Detectors for Astronomy VIII*. Ed. by Andrew D. Holland and James Beletic. Vol. 10709. Society of Photo-Optical Instrumentation Engineers (SPIE) Conference Series. July 2018, 107091H, 107091H. DOI: 10.1117/12.2311814.

[2] M. Feldt et al. "PYRAMIR: first on-sky results from an infrared pyramid wavefront sensor". In: *Society of Photo-Optical Instrumentation Engineers (SPIE) Conference Series*. Ed. by Brent L. Ellerbroek and Domenico Bonaccini Calia. Vol. 6272. Society of Photo-Optical Instrumentation Engineers (SPIE) Conference Series. June 2006, 627218, p. 627218. DOI: 10.1117/12.671305.

[3] M. Feldt et al. "SUPY: an infrared pyramid wavefront sensor for Subaru". In: *Society of Photo-Optical Instrumentation Engineers (SPIE) Conference Series*. Ed. by Brent L. Ellerbroek and Domenico Bonaccini Calia. Vol. 6272. Society of Photo-Optical Instrumentation Engineers (SPIE) Conference Series. June 2006, 62722A, 62722A. DOI: 10.1117/12.671248.

[4] Olivier Guyon et al. "The compute and control for adaptive optics (CACAO) real-time control software package". In: *Proc. Soc. Photo-Opt. Instrum. Eng.* Vol. 10703. Society of Photo-Optical Instrumentation Engineers (SPIE) Conference Series. July 2018, 107031E, 107031E. DOI: 10.1117/12.2314315.

[5] Yutaka Hayano et al. "The laser guide star facility for Subaru Telescope". In: *Society of Photo-Optical Instrumentation Engineers (SPIE) Conference Series*. Ed. by Brent L. Ellerbroek and Domenico Bonaccini Calia. Vol. 6272. Society of Photo-Optical Instrumentation Engineers (SPIE) Conference Series. June 2006, 627247, p. 627247. DOI: 10.1117/12.672583.

[6] N. Jovanovic et al. "The Subaru Coronagraphic Extreme Adaptive Optics System: Enabling High-Contrast Imaging on Solar-System Scales". In: *Pub. Astron. Soc. Pacific* 127.955 (Sept. 2015), p. 890. DOI: 10.1086/682989. arXiv: 1507.00017 [astro-ph.IM].

[7] Takayuki Kotani et al. "The infrared Doppler (IRD) instrument for the Subaru telescope: instrument description and commissioning results". In: *Proc. Soc. Photo-Opt. Instrum. Eng.* Ed. by Christopher J. Evans, Luc Simard, and Hideki Takami. Vol. 10702. Society of Photo-Optical Instrumentation Engineers (SPIE) Conference Series. July 2018, 1070211, p. 1070211. DOI: 10.1117/12.2311836.

[8] Julien Lozi et al. "AO3000 at Subaru: combining for the first time a NIR WFS using First Light's C-RED ONE and ALPAO's 64x64 DM". In: *Adaptive Optics Systems VIII*. Ed. by Laura Schreiber, Dirk Schmidt, and Elise Vernet. Vol. 12185. Society of Photo-Optical Instrumentation Engineers (SPIE) Conference Series. Aug. 2022, 1218533, p. 1218533. DOI: 10.1117/12.2630634. arXiv: 2209.12981 [astro-ph.IM].

[9] Julien Lozi et al. "New NIR spectro-polarimetric modes for the SCExAO instrument". In: *Society of Photo-Optical Instrumentation Engineers (SPIE) Conference Series*. Vol. 11448. Society of Photo-Optical Instrumentation Engineers (SPIE) Conference Series. Dec. 2020, 114487C, p. 114487C. DOI: 10.1117/12.2562792.

[10] Julien Lozi et al. "SCExAO, an instrument with a dual purpose: perform cutting-edge science and develop new technologies". In: *Proc. Soc. Photo-Opt. Instrum. Eng.* Vol. 10703. Society of Photo-Optical Instrumentation Engineers (SPIE) Conference Series. July 2018, 1070359, p. 1070359. DOI: 10.1117/12.2314282. arXiv: 1809.08301 [astro-ph.IM].

[11] Julien Lozi et al. "Visible and Near Infrared Laboratory Demonstration of a Simplified Pyramid Wavefront Sensor". In: *Pub. Astron. Soc. Pacific* 131.998 (Apr. 2019), p. 044503. DOI: 10.1088/1538-3873/ab046a. arXiv: 1901.11165 [astro-ph.IM].

[12] Y. Minowa et al. "Performance of Subaru adaptive optics system AO188". In: *Adaptive Optics Systems II*. Vol. 7736. Proc. Soc. Photo-Opt. Instrum. Eng. July 2010, 77363N, 77363N. DOI: 10.1117/12.857818.

[13] Yoshito H. Ono et al. "Overview of AO activities at Subaru Telescope". In: *Society of Photo-Optical Instrumentation Engineers (SPIE) Conference Series*. Vol. 11448. Society of Photo-Optical Instrumentation Engineers (SPIE) Conference Series. Dec. 2020, 114480K, 114480K. DOI: 10.1117/12.2561139.

[14] G. Singh et al. "On-Sky Demonstration of Low-Order Wavefront Sensing and Control with Focal Plane Phase Mask Coronagraphs". In: *Pub. Astron. Soc. Pacific* 127 (Oct. 2015), pp. 857–869. DOI: 10.1086/682726. arXiv: 1506.06298 [astro-ph.IM].

[15] Hideki Takami et al. "Status of Subaru laser guide star AO system". In: *Society of Photo-Optical Instrumentation Engineers (SPIE) Conference Series*. Ed. by Brent L. Ellerbroek and Domenico Bonaccini Calia. Vol. 6272. Society of Photo-Optical Instrumentation Engineers (SPIE) Conference Series. June 2006, 62720C, p. 62720C. DOI: 10.1117/12.670568.

[16] Fabrice Vidal et al. “Tests and characterisations of the ALPAO 64×64 deformable mirror, the MICADO-MAORY SCAO AIT facility”. In: *Proceedings of the AO4ELT6 conference*. Nov. 2019, E4.

[17] S. Vievard et al. “Focal plane wavefront sensing on SUBARU/SCExAO”. In: *Society of Photo-Optical Instrumentation Engineers (SPIE) Conference Series*. Vol. 11448. Society of Photo-Optical Instrumentation Engineers (SPIE) Conference Series. Dec. 2020, 114486D, p. 114486D. DOI: 10.1117/12.2562787. arXiv: 2012.12417 [astro-ph.IM].